

Open camera or QR reader and scan code to access this article and other resources online.



Synergistical Mechanical Design and Function Integration for Insect-Scale On-Demand Configurable Multifunctional Soft Magnetic Robots

Xingxing Ke,* Haochen Yong,* Fukang Xu, Zhiping Chai, Jiajun Jiang, Xiang Ni, and Zhigang Wu

Abstract

Meso- or micro-scale(or insect-scale) robots that are capable of realizing flexible locomotion and/or carrying on complex tasks in a remotely controllable manner hold great promise in diverse fields, such as biomedical applications, unknown environment exploration, *in situ* operation in confined spaces, and so on. However, the existing design and implementation approaches for such multifunctional, on-demand configurable insect-scale robots are often focusing on their actuation or locomotion, while matched design and implementation with synergistic actuation and function modules under large deformation targeting varying task/target demands are rarely investigated. In this study, through systematical investigations on synergistical mechanical design and function integration, we developed a matched design and implementation method for constructing multifunctional, on-demand configurable insect-scale soft magnetic robots. Based on such a method, we report a simple approach to construct soft magnetic robots by assembling various modules from the standard part library together. Moreover, diverse soft magnetic robots with desirable motion and function can be (re)configured. Finally, we demonstrated (re)configurable soft magnetic robots shifting into different modes to adapt and respond to varying scenarios. The customizable physical realization of complex soft robots with desirable actuation and diverse functions can pave a new way for constructing more sophisticated insect-scale soft machines that can be applied to practical applications soon.

Keywords: soft magnetic robots, synergistical design, mechanical design, function integration, configurable robots

Introduction

BY THE VIRTUE of tiny bulk, agile response, and functionalized body, insect-scale robots may be ideal candidates for numerous attractive applications in various unstructured/extreme environments or when interacting with unknown

targets,¹ such as biomedical scenarios,^{2,3} exploration,⁴⁻⁶ *in situ* robotic operations in confined spaces, and other emerging applications.⁷ In the meanwhile, these significant application scenarios also put forward high requirements for the performance and functionalities of the adopted insect-scale robots,⁸ such as wireless actuation,⁹ distinct controllability,¹⁰

State Key Laboratory of Digital Manufacturing Equipment and Technology, Huazhong University of Science and Technology, Wuhan, China.

*These authors contributed equally to this work.

robust multifunction integration/configuration capability,¹¹ and so on.

Recent progress in materials and soft robots has enabled a plethora of smart actuators with diverse actuation mechanisms,^{12–21} such as photochemical/thermal effects,²² shape-memory alloy/polymers,²³ magnetic actuation,^{24–28} surface tension gradient²⁹ (Marangoni effects), biohybrid artificial muscles,³⁰ etc. These actuators render various insect-scale soft robots to realize effective locomotion and perform complex tasks in harsh environments,^{5,9} providing novel design routes and new possibilities for insect-scale soft robots. However, the in-depth interaction between the constructed insect-scale soft robots and the operated targets remains a challenge due to the unstructured/unpredictable work conditions of target scenes and limited configurability and functionalities (e.g., *in situ* multistimuli response, somatosensing, environment perception, multilocomotion transition, and other compatible multifunctionalities) of the constructed insect-scale soft robots. Such a challenge hinders their further applications of those insect-scale soft robots in those attractive scenarios.

Among those insect-scale soft robots, soft magnetic robots are an elegant yet promising solution to be competent in harsh and unstructured scenarios,¹ by the virtue of their untethered remote actuation,³¹ programmable,²⁴ addressable,³² and fast response³³ with high force and torques.³⁴ In recent years, quite a few elegant approaches were reported to construct such insect-scale soft robots.³⁵ For instance, Sitti and colleagues constructed a small-scale multimode magnetic robot that can locomote and perform different tasks with various modes.²⁵ Similarly, utilizing 3D printing methods, Zhao *et al.* and Diller *et al.* proposed a magnetized ink 3D direct printing approach to realize programmable small-scale soft robots²⁴ and develop an ultraviolet lithography-based printing method to construct millimeter-scale flexible robots with programmable three-dimensional magnetization and motions,³⁶ respectively. More recently, Shen and colleagues proposed a multilegged magnetic robot and agglutinate magnetic spray-enabled magnetic millirobots.^{37,38} Those approaches addressed magnetic domain encoding and precise actuation.

However, to further fulfill in-depth interaction between insect-scale soft robots and unstructured application scenarios, a few aspects must be accounted for: flexible motion manipulation, synergistic multifunction integration, and target-based on-demand configurability. Most previous approaches focused on realizing flexible motion manipulation, lacking of consideration of both matched mechanical design and function integration. This technique vacancy greatly limits the potential of small-scale soft magnetic robots and hence makes them unable to cope with complex interaction scenarios as stated earlier. To break through such a bottleneck, it is urgent to develop synergistically matched design methods for insect-scale soft magnetic robots in terms of both ideal mechanical response and stable functional integration.

In this study, we present a synergistical design method, particularly from functional skin to main bulk, and diverse cells to modular robots under large deformation, for on-demand configurable, multifunction integrated, insect-scale soft magnetic robots. To assure effective and yet matched actuation and function of each module and the whole robotic system, we systematically investigated the matched design of the modules in terms of their mechanical responsive behav-

iors and various functionalities. These soft magnetic robots are enabled by a modular configuration strategy by fast assembling various standardized functional modules (e.g., actuation modules, connecting modules, sensing modules, steering modules, and other functional modules) together according to targeted design demand. These functional modules are coupled by the bulk and surface or mutually.

Furthermore, with the newly presented method, we demonstrated a (re)configured insect-scale soft magnetic robot that can rapidly shift different configurations with different actuation modes and functions, enabling it to well adapt to different scenarios and perform corresponding tasks. Here lists a few, motion gait self-sensing during walking, environment temperature perception under thermal irradiation when crossing through sand, light illumination response during crawling through a narrow tunnel, and perception of ultraviolet exposure when synergistically cruising on a water pool. It is a proof of concept of fast customizing functionalized insect-scale robots, providing a convenient platform technique for the robotic community to fast configure soft magnetic robots with desirable motion/actuation modes and functionalities.

Materials and Methods

Material preparation, fabrication, and modeling

The main body of each module was made of c-PDMS (carbon black doped polydimethylsiloxane, PDMS) or m-PDMS (magnetic particle doped polydimethylsiloxane, PDMS). They are silicone base of PDMS (Sylgard 184; Dow Corning Corp.) blended with carbon black (XC72R; Cabot) at a weight ratio of 10:1:0.5 (silicone base: curing agent: carbon black), or so-called c-PDMS; and NdFeB micro magnetic particles (MQFB-B-20076-089; Magnequench) at a weight ratio of 20:1:40 (silicone base: curing agent: NdFeB particles), or so-called m-PDMS, respectively. The prepared mixture was mixed by a digital stirrer (RW 20; IKA) at 2,000 rpm for 3 min and then vacuumed for 5 min to remove the bubbles. The functional cells were fabricated following the procedure described in Supplementary Figure S1. Among them, the c-PDMS are mainly used as structural parts and do not perform drive functions in the robot's motion.

The inclusion of carbon black in PDMS is to facilitate the use of laser processing. No evident material failure is observed after 10,000 cycles. More details can be seen in the Supplementary Data. The samples for the mechanical model fitting: the specimens with length (a) of 5 mm, width (b_a) of 1.5 mm, thickness (t_a) of 0.4 mm were made of m-PDMS at a weight ratio of 20:1:40 (silicone base: curing particles: NdFeB particles). The magnetization angles (θ_m) are 0°, 15°, 30°, and 45°, respectively. Then, the obtained specimens were coated by PDMS 10:1 with different thicknesses (t_s) from 0.05 to 0.25 mm; we also set the $t_s = 0$ mm as a reference group. We measured the deflection (w/a) of the specimens with different θ_m (0°, 15°, 30°, 45°) and t_s (0, 0.05, 0.15, 0.25 mm) in an applied magnetic field of 1,000 Gs.

Magnetic characterization

The magnetic moment density of the m-PDMS film specimens was measured by a vibrating sample magnetometer (S-VSM; Quantum). To obtain the specimens, the

m-PDMS film with various NdFeB mass fractions from 26% to 80% was cut into squares (length of 2 mm, thickness of ~ 0.1 mm) through the laser, the default parameters are: laser scanning speed (v) of 150 mm/s, current (I) of 33.5 A, frequency (f) of 50 kHz, pulse width (Q) of 0.2 μ s. The laser parameters required for the experiments in this article are default values unless otherwise specified. The actual specimen thickness is shown in Supplementary Table S1. We measured the residual magnetization of m-PDMS film (mass fraction of 50%) under applied magnetic fields from 350 to 2,450 Gs (Supplementary Fig. S2A). In addition, the magnetization of the m-PDMS film with a mass fraction from 26% to 80% was measured under the applied magnetic field of 2,500 Gs (Supplementary Fig. S2B). The temperature in the cavity was set to 300 K for all measurements.

Mechanical characterizations

To study the mechanical response of the main body to the magnetic field and the constraint behaviors of the surface layer, several experiments were designed with gradient magnetic fields from 100 to 1,600 Gs with a gradient of 300 Gs (Supplementary Fig. S3). The specimens with lengths of 3, 5, and 7 mm (0.4 mm thickness) and the specimens with thicknesses of 0.2, 0.4, and 0.6 mm were prepared for the mechanical response of the main body. The specimens (length of 5 mm and thickness of 0.4 mm) with the skin layer (thickness of 0.05, 0.15, and 0.25 mm) and the specimens with the skin layer with Young's modulus of 0.23, 0.99, and 2.25 MPa (ratio of silicone base: curing agent by weight, respectively, 20:1, 10:1, and 5:1) (Supplementary Fig. S4) were prepared for constraint behaviors of the surface layer. All the specimens have a width of 1.5 mm. The horizontal deviation of each specimen was captured using an SLR camera (EOS R5; Cannon) and measured on a computer. The actual thickness of the specimens were measured in Supplementary Table S3.

Finite-element analysis

Finite element analyses (FEAs) were carried out using solid mechanics and magnetic fields and no current modules in COMSOL Multiphysics 6.0 to simulate the results of the experiments presented in corresponding sections. The results of FEAs are shown in Supplementary Figure S5. More details are shown in the Supplementary Data and Supplementary Table S4.

Surface characterizations

To study the effect of the laser parameters on the properties of the skin layer surface (ability to adhere to liquid alloy [LA]), a specimen (6 \times 6 matrix) with gradient parameters was prepared: laser scanning speed (v) from 500 to 2,500 mm/s, laser scanning space (k) from 0.005 to 0.16 mm. The contact angle of LA on every matrix element was measured separately with a drop shape analysis equipment (DSA25; KRUSS) at room temperature. For the dynamic contact angle measurement, the LA droplet was infused at a speed of 6 μ L/min and withdrawn at a speed of 12 μ L/min using a syringe pump (PUMP 11 ELITE Nanomite; Harvard Apparatus). Furthermore, the profiles of the LA circuit were characterized: the LA was transferred to the skin layer surface; designed width (W_d) of the circuit is 0.2, 0.3, 0.4, 0.5, 0.6, and 0.7 mm. The

sectional morphology of the LA circuit was captured by a super depth of field microscope (DSX 510; Olympus). All experiments were performed at room temperature of 20°C.

Electrical characterizations

To characterize the stability of the LA circuit, 10,000 cycles of bending were carried on using a universal material testing machine (ElectroPuls E1000; Instron). Both ends of the specimen were fixed on the machine, then, the machine moved forth and back with an amplitude of 2 mm at a frequency of 2 Hz. The resistance of the LA circuit was measured using an LCR meter (E4980AL; Keysight).

Demonstration setup

For reconfigured magnetic robot demonstration, the LA circuit was directly printed on the actuation cell whose surface was selectively tuned by laser to obtain different wettability toward LA, and the dynamic resistance data were recorded by a digital multimeter (34461A; Keysight). The thermal irradiation was produced by a heating lamp with 275 W. The white light stimulus was produced by a white light source (SOLA AM 5-LCR-VA; Lumencor patented technology). The ultraviolet stimulus was produced by an ultraviolet analyzer (ZF-1; Shanghai Chitang Electronics Co., Ltd.). These stimuli are to simulate the potential varying environment to demonstrate the perception and response behaviors of these configured soft magnetic robots.

Results and Discussion

Synergistical design of the module in terms of both mechanical behaviors and function integration is significant for constructing functionalized soft magnetic robots. Figure 1 shows the concept of matched design strategy by codesigning the whole cell (module) consisting of the skin layer (functional layer) and main body (bulk), among which the whole cell with functional skin achieves an ideal mechanical response behavior while the functional layer can stably work under large deformation. To guarantee the above behaviors smoothly, on one hand, we proposed a matched design method by adjusting the matching relationship between the external magnetic field, \mathbf{B} , magnetization angle, θ_m , thickness of the skin layer, t_s , and Young's modulus, E_s , to achieve the target deformation. On the other hand, selecting the typical and commonly used functional ink (LA) as functional materials, we systematically studied its selective, yet stable integration on such a soft magnetic cell surface by introducing a laser surface tuning mechanism that can be precisely modeled by its removing energy, E_r .

Such a synergistic design of a single cell can further enable the modular functionalized soft magnetic robots by assembling various matched designed functionalized cells together, for example, integrating various functions on the main body surface such as optical sensor, thermal sensor, and LA functional circuit, empowering them with diverse specific capabilities, Figure 1E. Moreover, discrete magnetic domain encoding in each module enables the bulk responses to external magnetic fields, and the synergy work between different cells realizes the motion and function of the robot. The modules in a standard part library are classified into connection modules and actuation modules with different

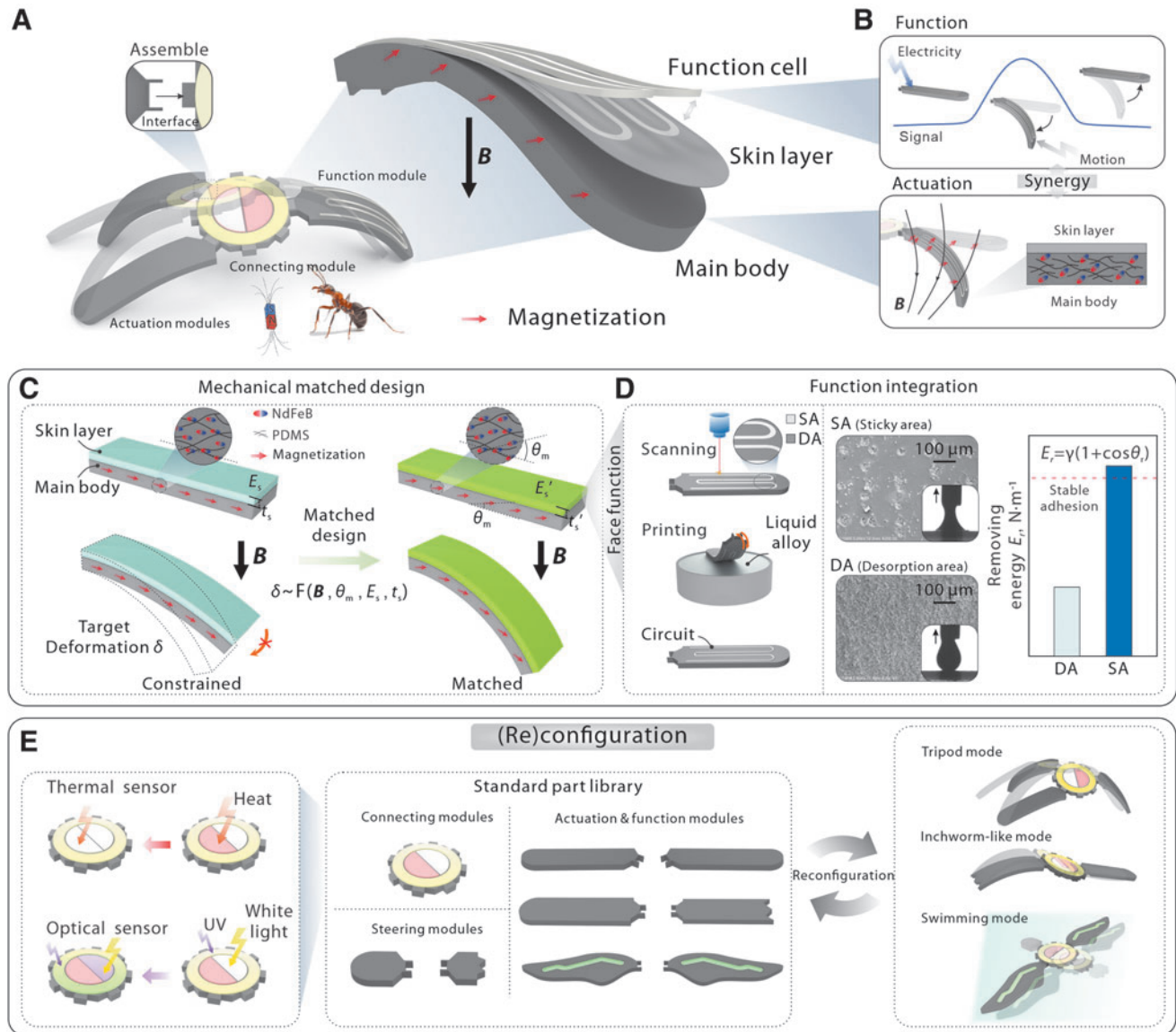


FIG. 1. Synergistical mechanical matched design and function integration, and its implementation demonstration on reconfigurable soft modular magnetic robots for various specific task scenarios. **(A)** Concept of the soft magnetic robot enabled by synergistically-designed cell. Various modular functional cells (e.g., connecting module, actuation module, and function module) realize the actuation and function of the robot with an external magnetic field. The matched design between the skin layer with the functional cell and the main body enables the robot to perform as anticipated. **(B)** Function cells on the skin can sense the motion, and the programmed magnetic domains enable the whole one to be actuated by an external magnetic field. **(C)** The concept and principles of mechanical matched design, when a functional layer is integrated on the surface of the magnetized main body (bulk), target deformation δ is related to an external magnetic field, B , magnetization angle, θ_m , the thickness of the skin layer, t_s , and Young's modulus, E_s . **(D)** The concept and principles of function integration, laser scanning the surface to obtain a stable SA and DA, respectively. The SA has greater removing energy, E_r , related to surface tension, γ , and receding angle, θ_r . **(E)** Concept of reconfigurable soft magnetic robots shifting into different modes enabled by the modules of the standard part library with various functions. DA, desorption area; SA, sticky area.

functions. The interface between the connection cell and the actuation cell is designed to facilitate reconfiguration, which further enables the robot to be customized and functionalized targeting diverse specific demands.

Matched mechanical response design

The structure design, magnetic domain presetting of actuation modules directly determines their response behaviors.

First, we systematically studied the effects of various structural parameters (thickness, t_a , and length, a) and magnetization angle (θ_m) on the magnetic response of the main body (deflection, w/a) under various strengths of magnetic fields. As in Figure 2 and Supplementary Figure S6A and B, the results indicate that the magnetic deflection, w/a , monotonically increases with the magnetic field B at various structural parameters and magnetization angle. The trend shows that smaller t_a and longer a will lead to a more ideal magnetic

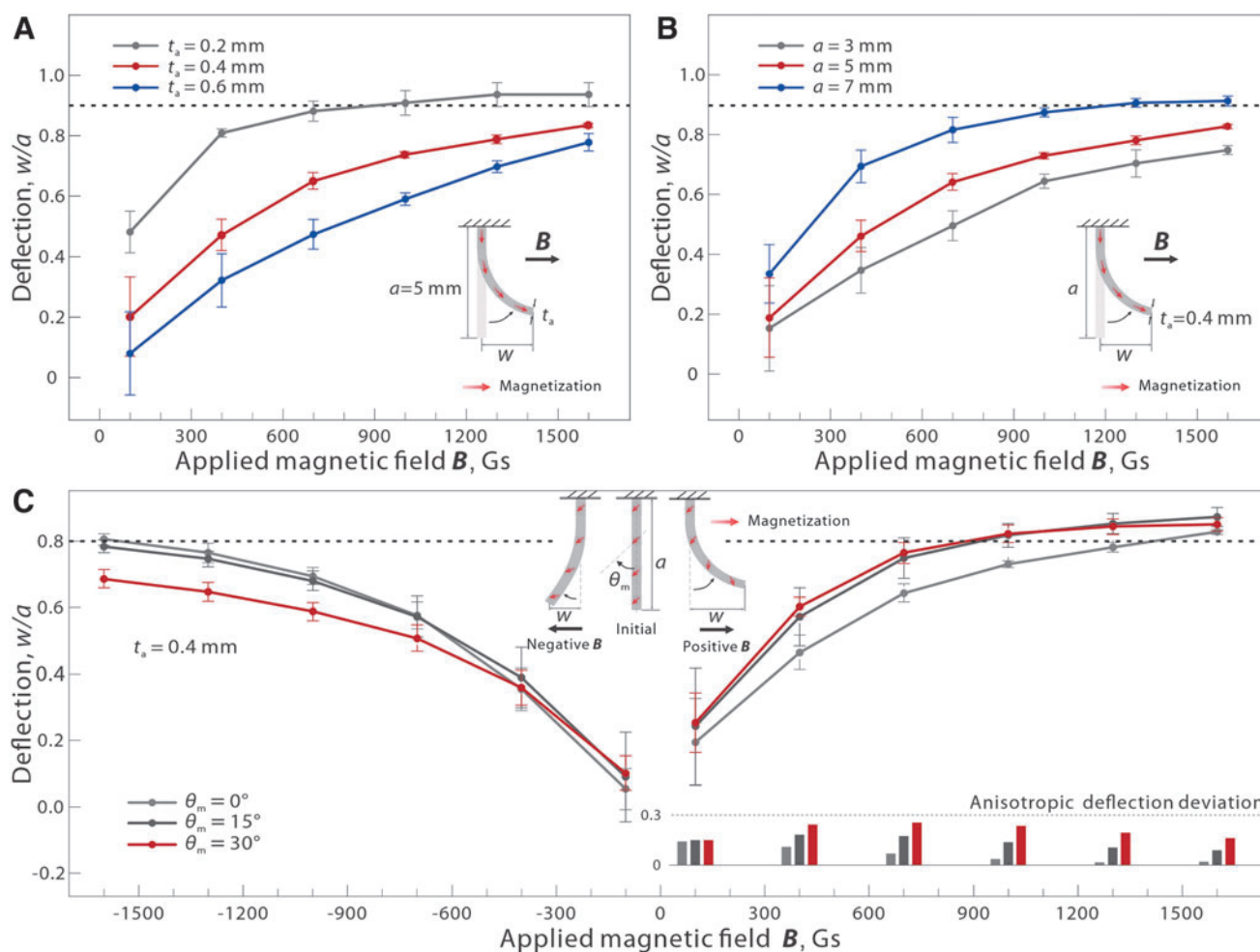


FIG. 2. Response characterizations of the original soft magnetic actuators without integrated functional skin. (A) The original response of soft magnetic actuators with the same length ($a=5$ mm) and different thicknesses, where w is the deflection of the endpoint. (B) The original response of soft magnetic actuators with the same thickness ($t_a=0.4$ mm) and different lengths. (C) The original response of soft magnetic actuators under different magnetization angles (θ_m), where B is the external magnetic field. The positive and negative signs of the applied magnetic field B just represent the direction of the applied magnetic field B , the applied magnetic field is increased from 100 to 1600 Gs in both positive and negative directions.

response that is described by the magnetic deflection, w/a . This can be explained by that the thickness, t_a , and length, a , will directly determine the bending stiffness of the whole cell. Therefore, within a certain range, deflection, w/a , decreases as thickness, t_a , and deflection, w/a , increases as length, a , under the same magnetic field, Figure 2A and B.

What's more, we found that the presetting of magnetic domain (magnetization angle, θ_m) in the bulk was significant for the response characterizations under the same actuation conditions (Notice that θ_m is defaulted as 0 in the in-plane magnetization case, if the out-of-plane magnetization was adopted, this magnetization angle would influence the magnetic response behaviors). The different magnetization angle, θ_m , leads to the anisotropic difference in the bending of the two sides, Figure 2C and Supplementary Figure S6C, which brings new design windows for the control of magnetic response. It means that by encoding such a parameter, we can obtain a better magnetic response behavior under limited or the same actuation conditions.

At the same time, we have verified the experimental results by FEA, Figure 3. The results indicate that when the θ_m is

$\sim 15^\circ$ – 30° , the strengthening effect on positive direction deflection is maximum. The simulation and experimental results have the same trend with some systematic errors. This tunable magnetization strategy provides a broaden design window for the addressable magnetic response programming of insect-scale soft robots.

Functional skin integrated onto the main body will influence its magnetic response. In this study, to make a matched mechanical design, we characterized the mechanical effects of skin attached on the main body quantitatively. The PDMS with various thicknesses, t_s , and Young's modulus, E_s (tuned by the mass ratio of precursors, Supplementary Fig. S4), was used to approximate the functional skin on the main body. The results indicate that the attached skin will cause a smaller magnetic deflection under the same magnetic field, Figure 4 and Supplementary Figure S6D and E. Therefore, for a practical functionalized main body, it is necessary to consider their comprehensive stiffness to obtain a better response. For instance, if there was a main body (t_a of 0.4 mm, a of 5 mm) with a skin (t_s of 0.15 mm, E_s of 0.99 MPa), to achieve the same deflection, w/a of ~ 0.6 , the magnetic field should be

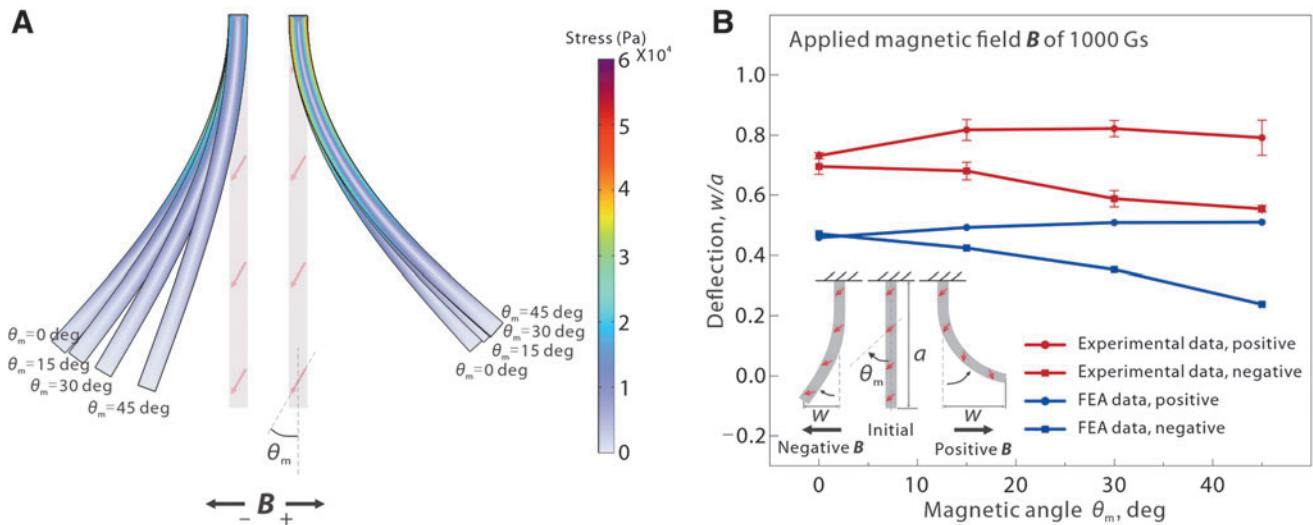


FIG. 3. Simulated different magnetization angles. **(A)** The result of different magnetization angles (θ_m from 0° to 45°). The strength of the external magnetic field B is 1,000 Gs. **(B)** Comparisons of experimental results with FEA results. FEA, finite element analysis.

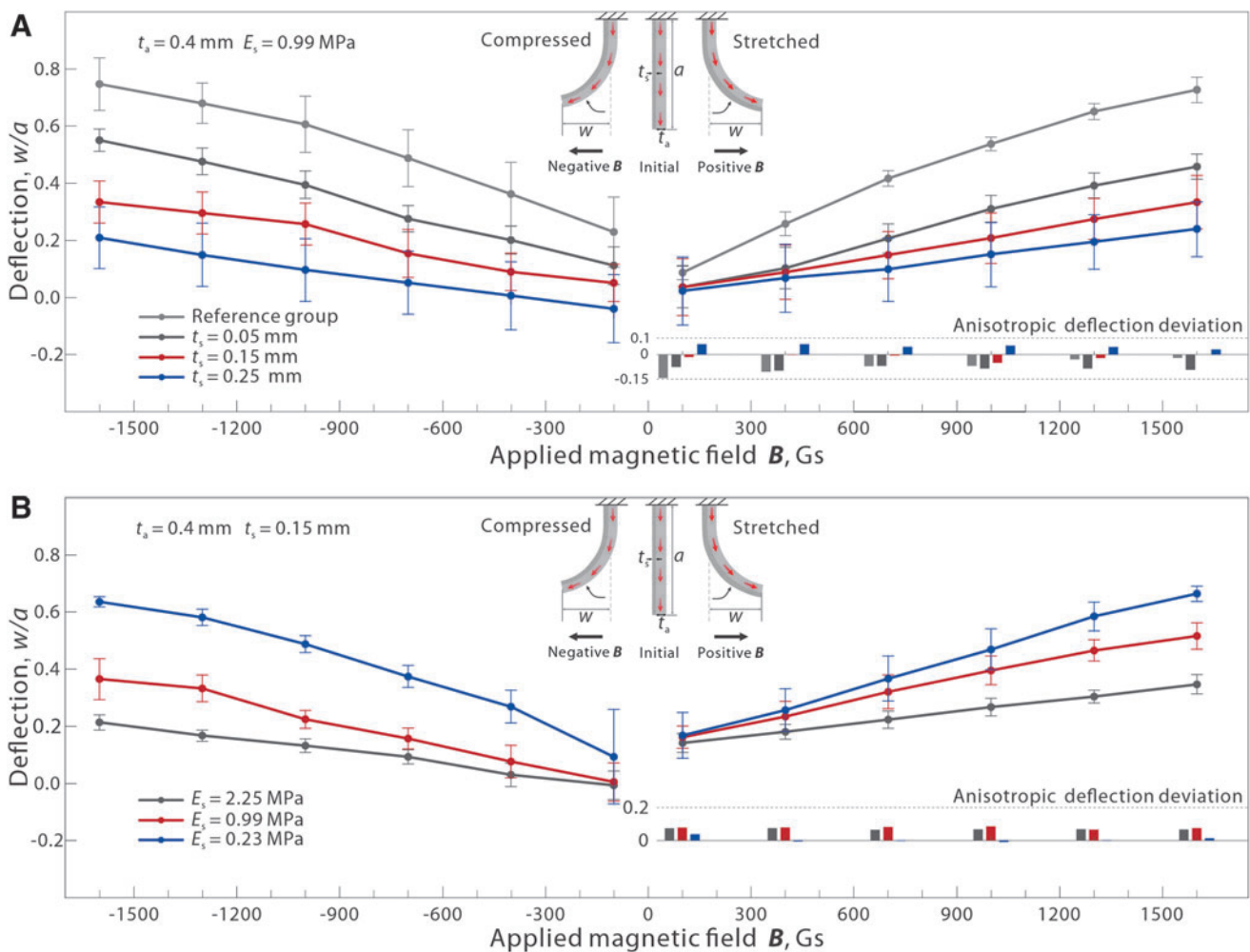


FIG. 4. Mechanical matched design of soft magnetic actuators with attached/coated skin. **(A)** The response of the actuators coated by the same skin materials (PDMS with a mass ratio of 10:1) with different thicknesses, t_s . w is the deflection of the endpoint. **(B)** The response of the actuators coated by the skin with different Young's modulus, E_s , where a is the length of the specimen equal to 5 mm. PDMS, polydimethylsiloxane.

increased from 100 to 1,600 Gs compared to the one without skin, alternatively, optimizing the structural parameters and magnetization angle, θ_m .

Because of the residual stress during the skin curing, the bulk has an original deflection and leads to the anisotropic deflection deviation (bottom right of Fig. 4). Furthermore, we verified the experimental results with numerical simulation, Figure 5. The results indicate that the simulation results are fairly consistent with the actual results. Such a synergistic mechanical design needs to comprehensively consider functional stiffness introduction and a matched strengthening by optimizing the materials' stiffness, structural parameters, magnetization strength, and magnetization angle.

As skin layers can somehow limit the actuation performance of the main body, we selected two key parameters that are easy to tune to establish the model, that is, by adjusting the magnetic angle (θ_m) to optimize/compensate the influence on the actuation of the main bulk caused by skin layer. The model can guide matched mechanical design. It is important to note that previous work has studied the mechanics of hard-magnetic soft material³⁹; it is still difficult to obtain an analytical solution under large deformation conditions. In this study, considering the skin layer as the same material as the main body, we derive an empirical formula based on the experimental results.

As shown in Figure 6A, B and Supplementary Figure S9, τ denotes the torque density, θ_m denotes the magnetization angle, w_{\max} denotes the max deflection in y direction, a denotes the length of the actuator, and t_s and t_a denote the thickness of the skin layer and main body. The magnetic torque at position s can be expressed as,

$$\tau(s) = |\mathbf{M}||\mathbf{B}|b_a t_a \int_s^a \sin\left(\frac{\pi}{2} - \theta + \theta_m\right) ds, \quad (1)$$

where \mathbf{M} and \mathbf{B} denote the magnetization of the actuator and the applied magnetic field, respectively, b_a denotes the width of the actuator, and θ is the deflection angle at the s . Abstracting the actuator as a cantilever beam and considering the skin layer and the main body as a whole, the curvature of the point s , $k(s)$ can be written as,

$$k(s) = \frac{\tau(s)}{EI}, \quad (2)$$

where $I = b_a(t_a + t_s)^3/12$ is the area moment of inertia, E is the Young's module, and μ is the shear modulus, which equals $1/3E$ for incompressible materials. The curvature $k(x)$ can be further written as,

$$k(s) = \frac{d\theta}{ds} = \frac{4|\mathbf{M}||\mathbf{B}|b_a t_a \int_s^a \sin\left(\frac{\pi}{2} - \theta + \theta_m\right) ds}{\mu(t_a + t_s)^3}. \quad (3)$$

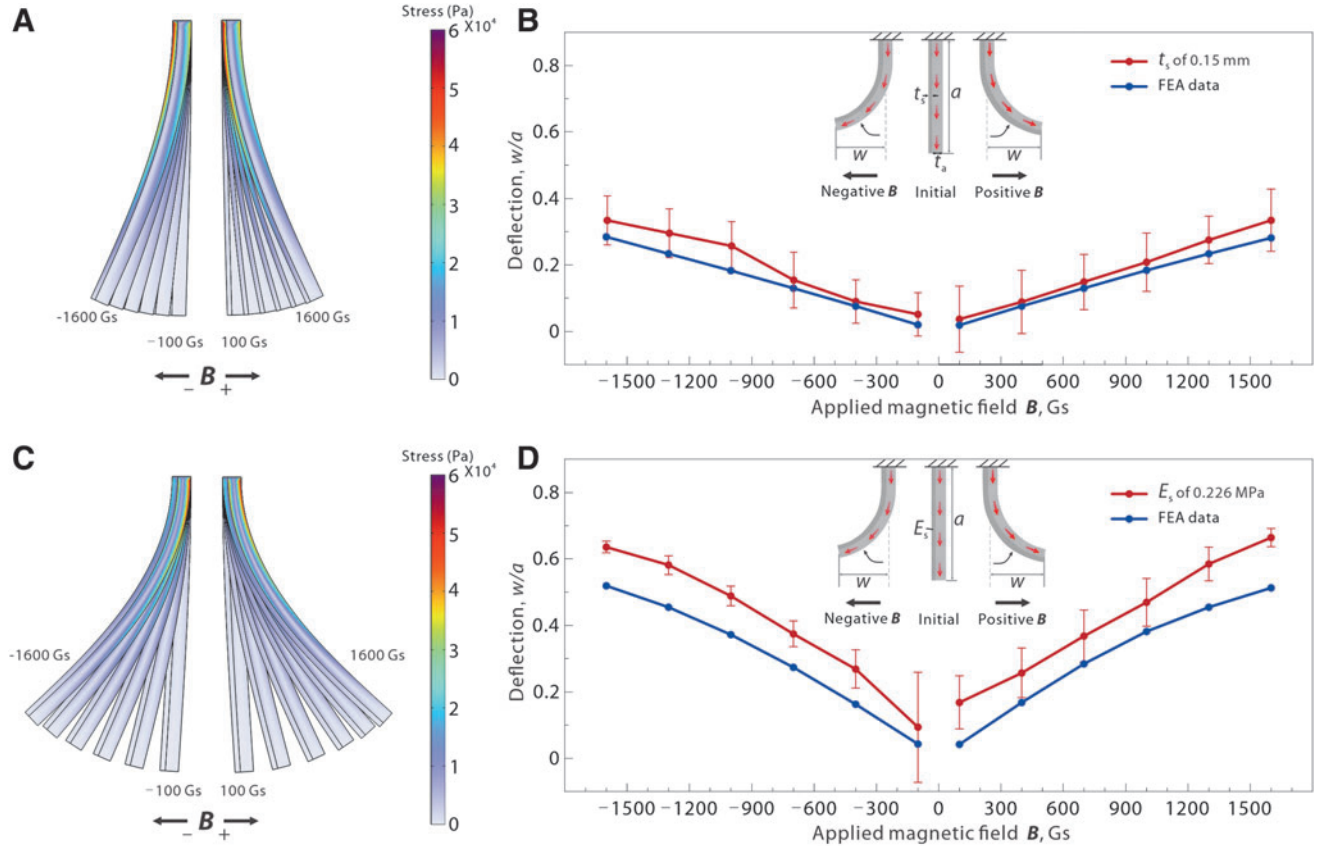


FIG. 5. Simulated different parameters of the skin layer. (A) The result of different magnetic strengths (from 100 to 1,600 Gs), the thickness of the skin layer t_s is 0.15 mm, and Young's modulus of the skin layer E_s is 0.9924 MPa. (B) Comparisons of experimental results with FEA results (t_s of 0.15 mm, E_s of 0.9924 MPa). (C) The result of different magnetic strength (from 100 to 1,600 Gs), Young's modulus of the skin layer E_s is 0.226 MPa, and the thickness of the skin layer, t_s , is 0.15 mm. (D) Comparisons of experimental results with FEA results (t_s of 0.15 mm, E_s of 0.226 MPa).

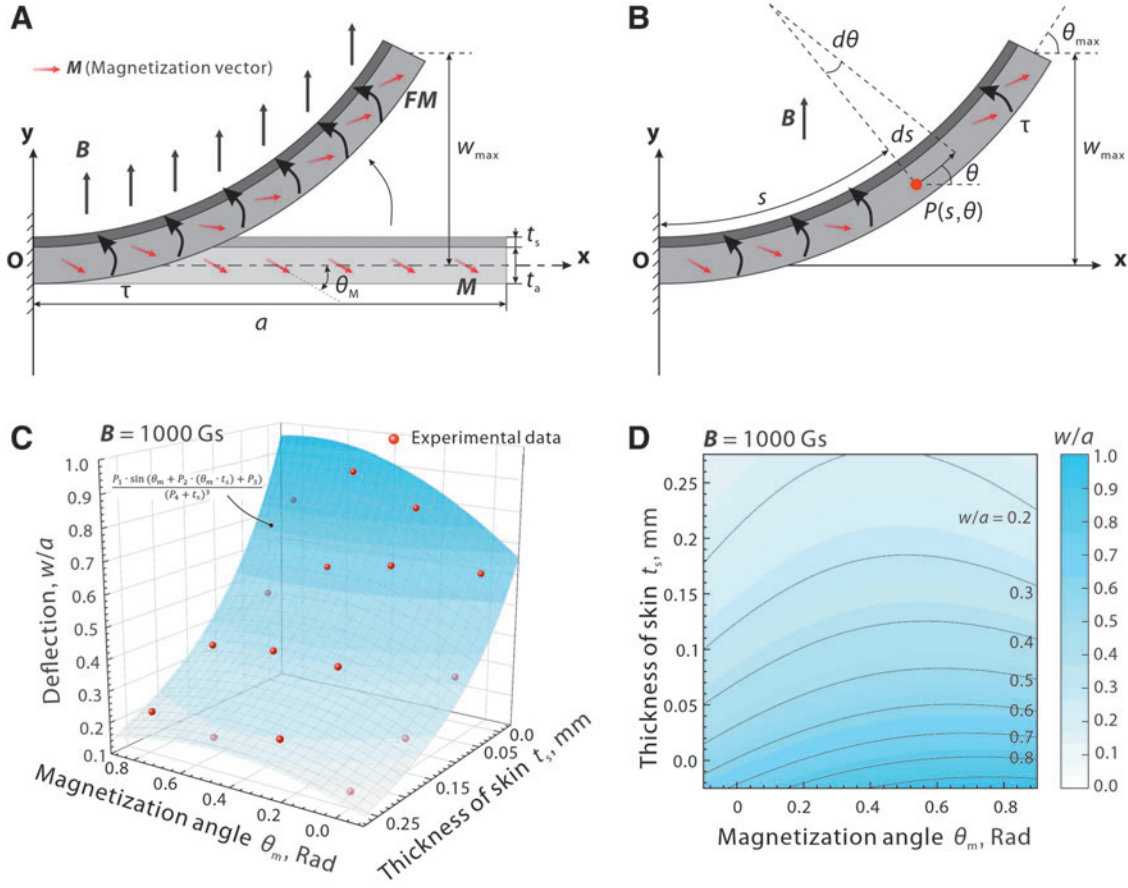


FIG. 6. Matched mechanical modeling for skin-coated/constrained functionalized soft magnetic actuators. **(A)** Actuator deforms under the applied magnetic field \mathbf{B} . Symbol \mathbf{M} denotes the magnetization of the actuator, \mathbf{F} denotes the deformation gradient tensor, a denotes the length of the actuator. **(B)** Geometry of the deformed actuator is characterized by a parameterized spatial curve $\theta = \theta(s)$, where s and θ represent the arc length and tangential angle at the spatial point, respectively. The rotation angle at the free tip is denoted as θ_{\max} . **(C)** Deflection (w/a) of the specimens with different θ_m ($0^\circ, 15^\circ, 30^\circ, 45^\circ$) and t_s (0, 0.05, 0.15, 0.25 mm) in an applied magnetic field of 1,000 Gs, where $P_1=0.08316$, $P_2=2.348$, $P_3=0.8413$, and $P_4=0.467$ are the fitting parameters and adjusted R -squared=0.8953. The applied magnetic field $\mathbf{B}=1,000$ Gs. **(D)** Relationship between θ_m and t_s , for a given thickness, the actuator response can be enhanced by properly adjusting θ_m .

Furthermore, from the geometric relationship we can obtain,

$$dy = \sin\theta \cdot ds. \quad (4)$$

$$w_{\max} = \int \sin(\theta(s)) \cdot ds \Big|_{s=a}, \quad (5)$$

where $\theta(s)$ is determined by Eq. (3), which cannot be written as an analytic solution. If we consider it in a small deflection model,²⁴ Eq. (1) can be written as:

$$\tau(x) = |\mathbf{M}||\mathbf{B}|b_a t_a (a-x) \sin\left(\frac{\pi}{2} + \theta_m\right). \quad (6)$$

The curvature of the point s $k(x)$ can be written as,

$$k(x) = \frac{\left|\frac{d^2y}{dx^2}\right|}{\left[1 + \left(\frac{dy}{dx}\right)^2\right]^{\frac{3}{2}}} = \frac{4|\mathbf{M}||\mathbf{B}|t_a(a-x)\sin\left(\frac{\pi}{2} + \theta_m\right)}{\mu(t_a + t_s)^3}. \quad (7)$$

When in a small deflection, $dy/dx \ll 1$, so Eq. (7) is approximately equal to

$$\frac{d^2y}{dx^2} = \frac{4|\mathbf{M}||\mathbf{B}|t_a(a-x)\sin\left(\frac{\pi}{2} + \theta_m\right)}{\mu(t_a + t_s)^3}. \quad (8)$$

Then, integrating Eq. (8), the deflection at the end can be obtained as,

$$w_{\max} = y|_{x=a} = \frac{4|\mathbf{M}||\mathbf{B}|t_a a^3 \sin\left(\frac{\pi}{2} + \theta_m\right)}{3\mu(t_a + t_s)^3}. \quad (9)$$

In this study, considering the introduced errors under the large deflection, we designed an empirical formula with the above model configuration with multiple correction factors to approximately calculate such a deflection w_{\max} . Based on further analysis of the model, we found that some rules should be taken into consideration: (1) the deflection δ decreases as t_s increases when θ_m is fixed; (2) there should be an optimal magnetization angle θ_{m0} , which allows the maximum magnetic torque to be obtained by making \mathbf{B} as

perpendicular as possible to M at a balanced state, and when $\theta_m > \theta_{m0}$, the result of $M \times B$ will decrease; (3) the optimal magnetization angle θ_{m0} decreases as t_s increases.

Based on the above considerations, using a trigonometric function to represent an equivalent magnetic moment with consideration of θ_m and t_s , we developed an empirical formula as,

$$\delta = \frac{w_{max}}{a} = \frac{P_1 \cdot \sin(\theta_m + P_2 \cdot (\theta_m \cdot t_s) + P_3)}{(P_4 + t_s)^3}, \quad (10)$$

where P_1 – P_4 are the fitting parameters. Specifically, P_1 denotes the influence of some constants (e.g., applied magnetic field, magnetization, shear modulus), P_2 denotes the coupling relationship between θ_m and t_s , P_3 denotes the angle compensation, and P_4 denotes the thickness parameter of actuation body, t_a . By fitting the experimental data, we can obtain $P_1=0.08316$, $P_2=2.348$, $P_3=0.8413$, $P_4=0.467$, and adjusted R -squared=0.8953 (Fig. 6C, D). With such an empirical model, the targeted deflection response can be approximately obtained. Hereinafter, it is used for the matched mechanical design for the skin-coated functionalized soft magnetic robots/actuators.

Stable integration of functional skin

Another key scientific problem of matched design lies in the stability of functional skin integrated/attached on a soft actuation body which may suffer from a periodical large deformation. Our previous works have reported that micro- and nano-scale surface structures may play a crucial role in pinning LA circuits on PDMS surfaces.⁴⁰ Herein, as shown in Figure 7A, different surface structures were created by various laser operational parameters (scanning spacing, k , and scanning speed, v). We measured the contact angles (advancing contact angle, θ_a , and receding contact angle, θ_r) of LA droplets ($\sim 0.8 \mu\text{L}$) on several surfaces in the air (Fig. 7B). The results indicate that stable adhesion means a large θ_a and a small θ_r .

As in Figure 7C, according to the microscale surface structures of m-PDMS with different laser parameters and the shapes of LA droplets during withdrawal, we determined the boundary of different adhesion states. Unstable adhesion means that it is difficult for the LA to be pinned on the surface, and thus, the adhesion is very weak; stable adhesion means that it is easy to pin LA on the surface. It can be seen that when the $v > 1,000 \text{ mm/s}$, the surface shape of the LA (red line in Fig. 7C) during withdrawing changes from a

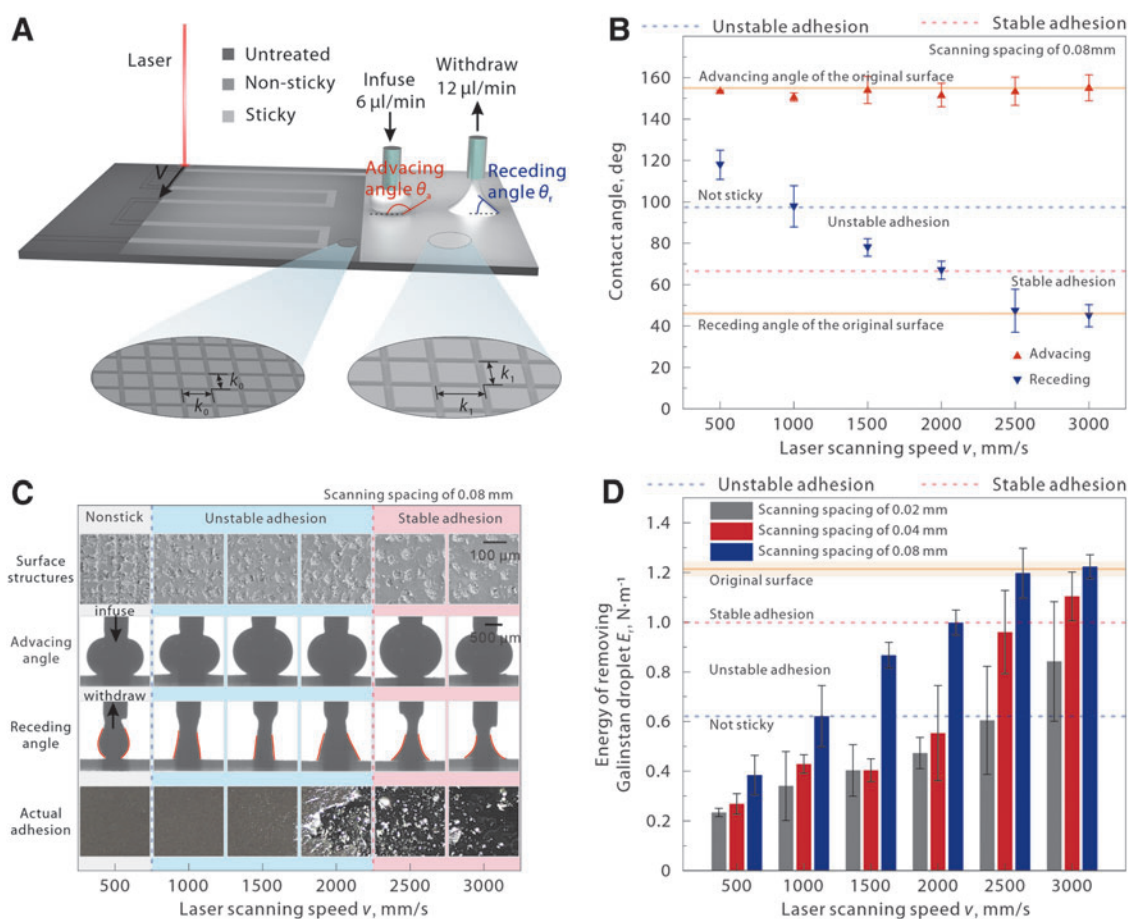


FIG. 7. Integration of the functional skin. (A) Schematic of surface laser patterning treatment, where v and k are the speed and spacing of the laser, respectively. (B) The advancing (θ_a) and receding (θ_r) angle of the LA droplet on the treated surface with k of 0.08 mm. (C) The surface-attached capability of soft magnetic actuator surface with different laser parameters; the rate for infusing and withdrawing are 6 and 12 $\mu\text{L}/\text{min}$, respectively. The surface shape is drawn with red lines. (D) The energy of removing LA droplet (E_r , the calculation details are in Supplementary Data) from the surfaces with different laser parameters. LA, liquid alloy.

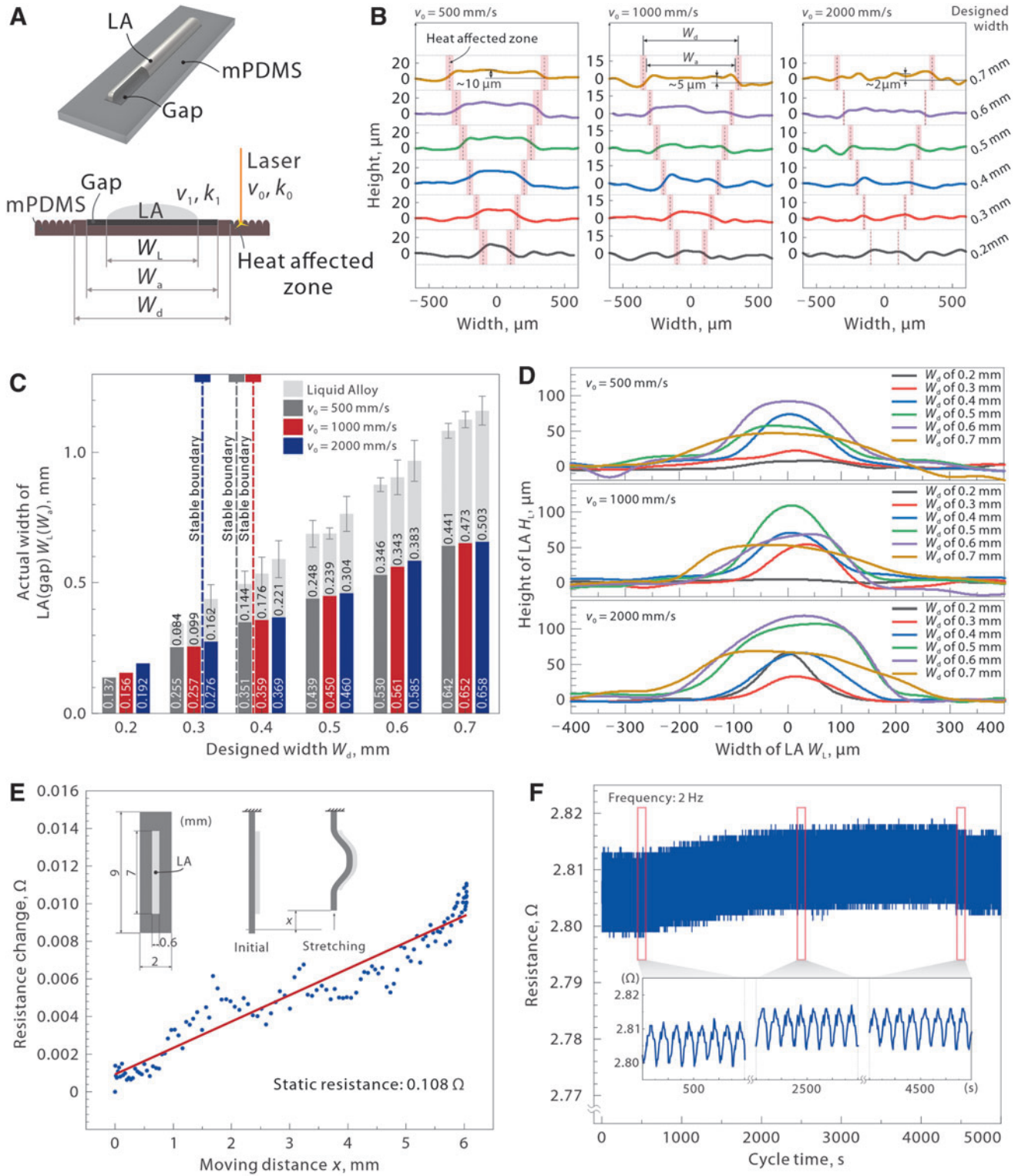


FIG. 8. Morphology and electrical properties of surface LA. **(A)** Schematic diagram of laser processing, where v_0 and k_0 are the scanning speed and spacing of the laser for no SA, v_1 and k_1 are the scanning speed and spacing of the laser for the gap (the gap was not treated by the laser in this test), W_d is the designed width, W_a is the actual width of the gap, and W_L is the actual width of the LA circuit. **(B)** Original surface profiles when the no SA is treated by different laser parameters. **(C)** The minimum widths for transfer printing characterizations of LA on diverse surfaces. **(D)** Surface topography profile for transfer printing characterizations of LA on diverse surfaces modified by laser. **(E)** Calibration of the relationship between the change of resistance and bending distance, x , where the static resistance is $\sim 0.1 \Omega$, for the LA circuit with a length of 7 mm and W_d of 0.6 mm, the resistance change due to bending is about 10%. **(F)** Fatigue testing of surface circuits (W_d of 0.6 mm), the test frequency is 2 Hz, and the cycling number is 10,000 times.

convex circle to a straight line, and when the v further increases to 2,500 mm/s, the surface shape further shrinks inward and becomes a concave curved surface. It reflects the process of increasing the adhesion force. Combined with the actual adhesion, we identified that the v equal to 1,000 and 2,500 mm/s is the boundary of the unstable adhesion and the stable adhesion, respectively, for our cases.

Furthermore, we calculated the removal energy (E_r , details in the Supplementary Data) of LA droplet through the receding angles. The results indicate that the smaller k , the smaller the removal energy, which makes the LA less likely to adhere with m-PDMS, Figure 7D. The regular pattern is verified by the experiments with different laser parameters (Supplementary Fig. S7). According to the above results, it can provide us a rapid selective integration method for diverse functional circuits.

As in Figure 8A, the surface of the main body was treated by different laser parameters to obtain different surface morphologies that showed a nonsticky state (k_0 and v_0) and stable adhesion state (k_1 and v_1 , here is the original surface without treatment), respectively. We observed the surface profiles after laser scanning with different parameters, Figure 8B. The results indicate that the actual width (W_a) of gap is smaller than the W_d because of the heat-affected zone. Non-negligible facula and ablation effect of the laser beam result in a larger non-sticky area (SA) and smaller SA.⁴¹

Furthermore, we observed the surface profiles after adhering to LA. The profile results in Figure 8C show that the

LA width (W_L) and W_a increase as the increase of W_d . It can be found that when the v_0 increases from 500 to 2,000 mm/s, the minimum widths of W_d will decrease about ~ 0.1 mm. Furthermore, we use a linear function, $y = ax + b$, to fit the linear relationship between the design width (W_d) and the W_a , design width (W_d) and the width of the liquid metal (W_L), respectively, to provide clearer guidance for the integration of the more sophisticated functional layer. All the fitted parameters are listed in Supplementary Table S2. Finally, we recorded the cross-sectional topography of the LA, Figure 8D, and analyzed the characteristic parameter H_L/W_L (Supplementary Fig. S8); higher H_L/W_L means taller and narrower cross-sectional topography. The result indicates that H_L/W_L decreases along as W_d with the laser parameters v_0 is of 2,000 mm/s and k_0 is of 0.02 mm.

However, when W_d is of 0.3 mm, H_L/W_L has a smaller value with the smaller v_0 indicating that the adhesion of LA is not sufficient at this time. It is further verified that the higher the laser thermal power, the larger the minimum line width of the gap on which the LA can be stably adhered. The above integration results provide us with clear guidance for our subsequent circuit design.

In addition, we also characterized the stability of its electrical characteristics. First, we measured the resistance change of a single LA circuit which is as a function of the bending deformation of the main body, Figure 8E. The static resistance is $\sim 0.1 \Omega$, for the LA circuit with a length of 7 mm

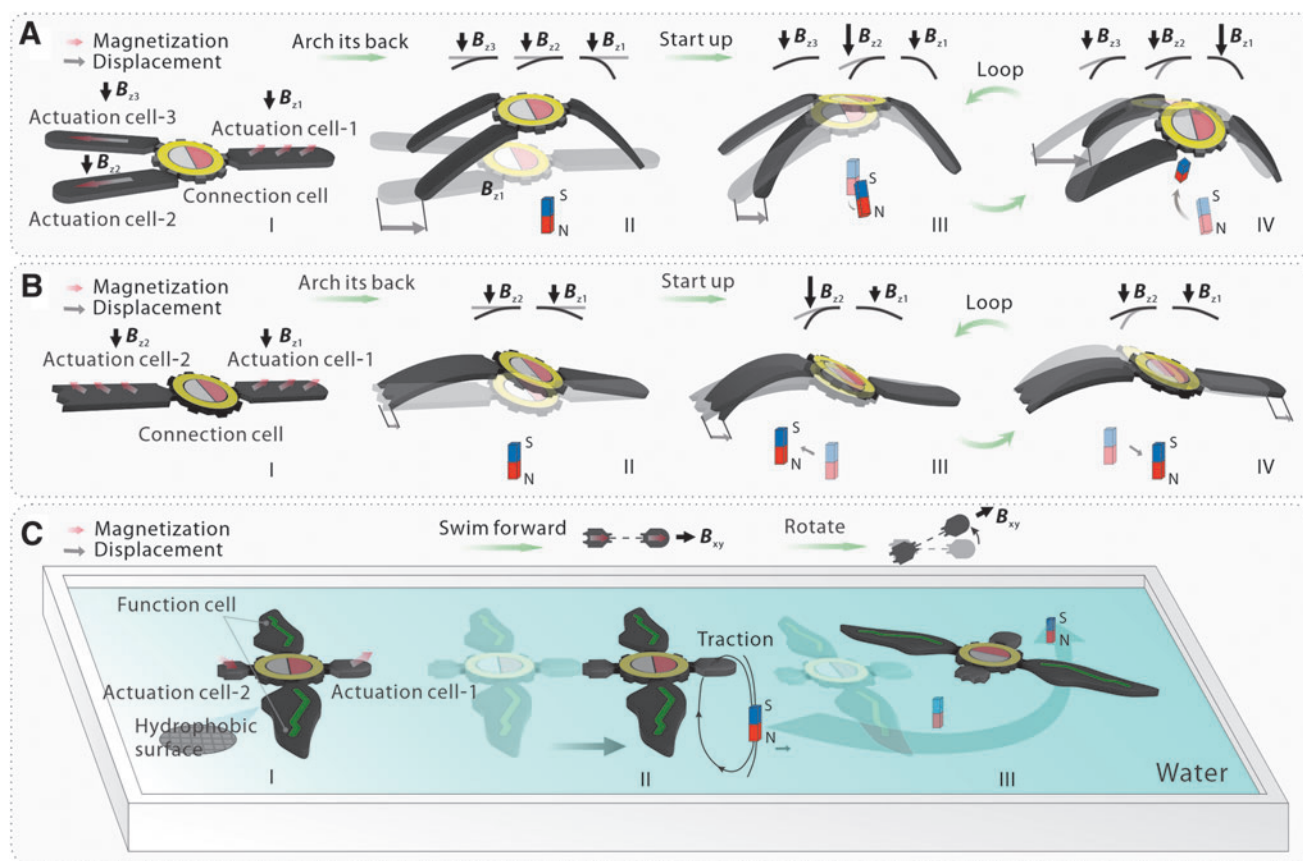


FIG. 9. Modular synergy for effective locomotion. (A) Tripod mode, the magnet moves in a plane perpendicular to the advancing direction to drive the robot forward. (B) Inchworm-like mode, the magnet moves in a plane parallel to the advancing direction to drive the robot forward. (C) Swimming mode, hydrophobic treatment of functional cells allows the robot to float on water.

and W_d of 0.6 mm; the resistance change due to bending is about 10%. To determine the stable electrical performance of the LA circuit, 10,000 bending fatigue tests were performed at a frequency of 2 Hz, Figure 8F, and the reference resistor has $\sim 5\%$ drift ($\sim 0.005 \Omega$).

Synergized modular robot design and demonstrations

The mutual cooperation of different modules realizes the overall motion of the robot. Figure 9A shows the motion control of the tripod mode: (1) initial state, actuation cell-1 has a θ_m ; (2) when a magnet is placed under its bottom, the robot arches its back; (3) when the magnet moves toward actuation cell-2 in a plane perpendicular to the advancing direction, the magnetic force received by actuation cell-2 increases, and the magnetic force received by actuation cell-3 decreases, while simultaneously, the contact point between actuation cell-2 and the ground will move forward due to greater bending deformation, while actuation cell-1 is almost unchanged due to the θ_m ; (4) the magnet moves to the other side, so that the contact point between actuation cell-3 and the ground advances, and this cycle realizes the movement.

Similarly, for the inchworm-like mode in Figure 9B, both actuation cells have a θ_m , so that the robot can better follow the direction of the magnetic field lines in space. The magnet moves in a plane parallel to the direction of advancement, thereby driving the robot forward. For such a low-frequency crawling motion, the slight response delay can be ignored,¹

and the delay is <2.5 ms under our operating conditions (Supplementary Fig. S10). For the swimming mode, by applying laser hydrophobic treatment to the bottom surface of the function cell, the robot can float on the water surface, actuation cells provide the driving force in the magnetic field, and magnetic domain orientation enables robot orientation, Figure 9C.

Inspired by the flexible reconfiguration strategy of LEGO's toys, we design a series of standardized cells with specific magnetic domains and functionalities, Figure 10A. All the cells are designed with standardized joints/interfaces for the convenience of reconfiguration. The targeted magnetic robot can be offline (re)configured into desirable structures, Figure 10B, to adapt to diverse scenarios as follows:

- (i) A tripod magnetic robot was configured, where an LA circuit was integrated and it can perceive its locomotion gait information. Based on the cyclically varied resistance fluctuations, we can recognize its relative high-frequency motion (~ 0.67 Hz), rest state, and relative low-frequency motion (~ 0.33 Hz).
- (ii) To eliminate the signal cables, we reconfigured its front leg into a magnetic leg cell and retain the rest part to turn into an untethered magnetic robot. Since thermal, optical sensitive ink and quantum dots were introduced onto the middle cell, the tripod magnetic robot can perceive high temperature by showing

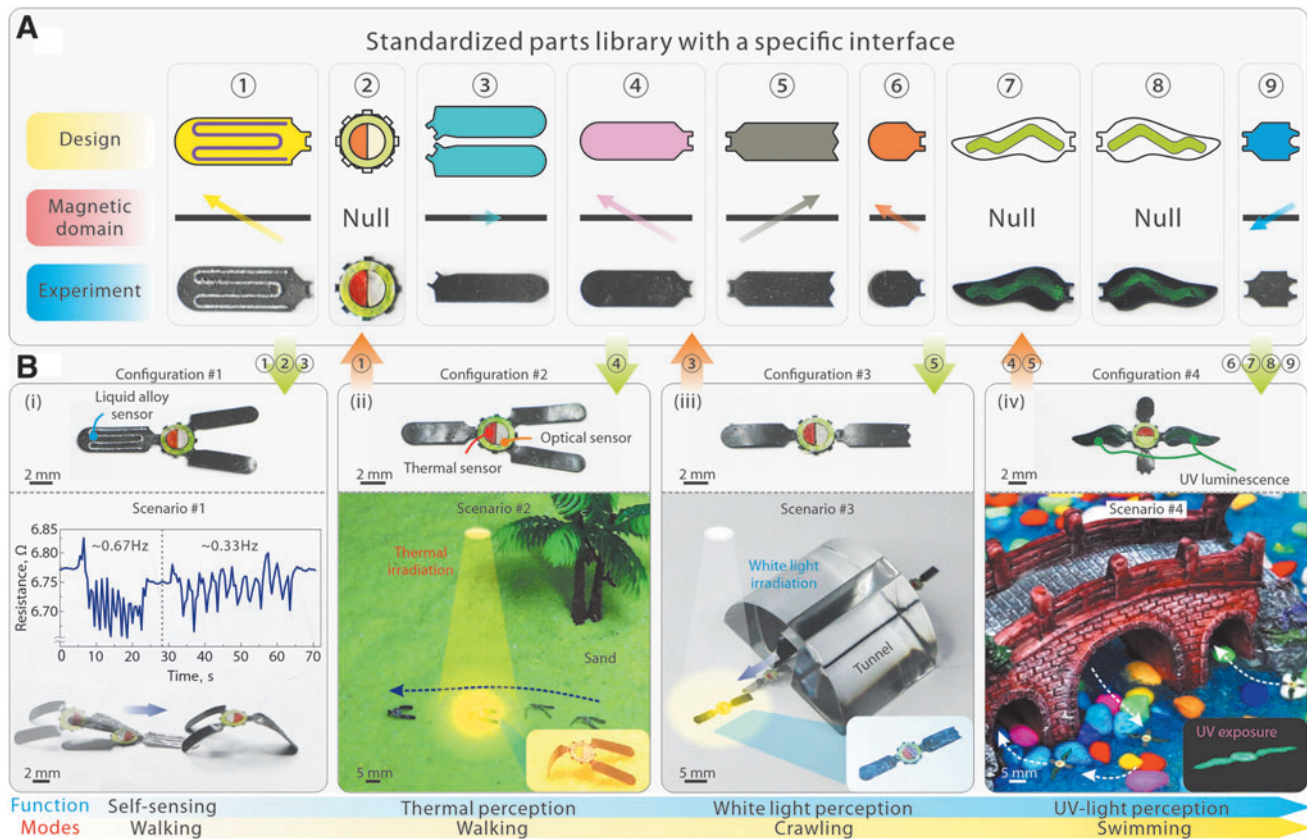


FIG. 10. Demonstrations of (re)configurable soft modular magnetic robots. (A) Standardized parts library with a specific interface. (B) Configurable soft magnetic robots shift into different modes to adapt and respond to varying scenarios: (i) self-sensing of movement, (ii) walking on the sand and sensing ambient temperature, (iii) crawling in the tunnel and sensing the ambient white light radiation, (iv) swimming on the water and sensing the UV-light radiation. UV, ultraviolet.

color change through the corresponding part from orange-red to yellow while it crossed the sand.

- (iii) To cross through a narrow tunnel, we reconfigured the tripod robot into an inchworm-like robot by replacing its back legs with a single leg to change its shape and gait. Analogously, it can perceive the sunlight by showing a color change of the corresponding part from white to purple.
- (iv) To cruise on a water environment, we reconfigured the inchworm-like robot into a swimming robot by replacing its legs with corresponding actuation/orientation and ultraviolet-responsive wing cells that have been pretreated into superhydrophobic on the lower surface for low flow friction when contacted to water. The swimming robot can achieve controllable movement oriented with specific magnetic domains under the actuation of the magnetic attraction and trace amount of surfactant, and shows luminescence coloration in an ultraviolet illumination.

These robots can be offline reconfigured to change their configuration based on specific demands at a relatively low cost, which indicates that it may serve as a feasible strategy for magnetic robots to adapt their behaviors in different potential scenarios, Supplementary Video S1.

Conclusions

In brief, to obtain codesigned functionalized insect-scale soft magnetic robots, herein, we report a synergistical design method of actuation bulk and functional skin in terms of both matched mechanical response and stable function integration. Specifically, focusing on this perspective, a systematical investigation was conducted: (1) a matched mechanical design method was studied based on the experiments and finite element analysis, that is, the bending stiffness introduced by different attached surface functional layers can be described by Young's modulus, E_s , and thickness, t_s , and their comprehensive magnetic response behaviors can be synergistically designed and compensated by tuning the magnetization strength/direction and applied magnetic fields; and (2) appropriate laser processing windows for rapidly and selectively integrating LA circuits were found, enabling stable integration of LA functional layer. Based on this designed method and a modular configuration strategy, we demonstrated that diverse soft magnetic robots can be configured to adapt to different scenarios with desirable motion and function.

This work realizes customizable, matched designed insect-scale soft magnetic robots with desirable actuation and function, which can pave the way toward constructing more sophisticated insect-scale soft machines that can be applied to numerous attractive applications, such as adaptively interacting with unknown targets, biomedical scenarios, exploration, *in situ* robotic operations in confined spaces, and other emerging applications.

Authors' Contributions

X.K. and Z.W. conceived this project. X.K., H.Y., F.X., Z.C., and J.J. carried out the experiments and characterizations. X.K., H.Y., and F.X. analyzed the data, interpreted the results, and developed the models. H.Y. and X.N. performed the simulation. X.K., H.Y., and Z.W. drafted the article.

X.K. and H.Y. contributed equally to this work. All authors participated in the discussions of the research.

Author Disclosure Statement

No competing financial interests exist.

Funding Information

This work was supported by the National Natural Science Foundation of China (52188102).

Supplementary Material

Supplementary Data
 Supplementary Figure S1
 Supplementary Figure S2
 Supplementary Figure S3
 Supplementary Figure S4
 Supplementary Figure S5
 Supplementary Figure S6
 Supplementary Figure S7
 Supplementary Figure S8
 Supplementary Figure S9
 Supplementary Figure S10
 Supplementary Table S1
 Supplementary Table S2
 Supplementary Table S3
 Supplementary Table S4
 Supplementary Video S1

References

1. Hines L, Petersen K, Lum GZ, *et al.* Soft actuators for small-scale robotics. *Adv Mater* 2017;29:1603483.
2. Zhang H, Li Z, Gao C, *et al.* Dual-responsive biohybrid neutroblots for active target delivery. *Sci Robot* 2020;6:eaa29519.
3. Nelson BJ, Kaliakatsos IK, Abbott JJ. Microrobots for minimally invasive medicine. *Annu Rev Biomed Eng* 2010; 12:55–85.
4. Yang X, Chang L, Pérez-Arancibia NO. An 88-milligram insect-scale autonomous crawling robot driven by a catalytic artificial muscle. *Sci Robot* 2020;5:1–14.
5. Li G, Chen X, Zhou F, *et al.* Self-powered soft robot in the Mariana Trench. *Nature* 2021;591:66–71.
6. Li T, Li G, Liang Y, *et al.* Fast-moving soft electronic fish. *Sci Adv* 2017;3:e1602045.
7. Zhou C, Yang Y, Wang J, *et al.* Ferromagnetic soft catheter robots for minimally invasive bioprinting. *Nat Commun* 2021;12:1–12.
8. Hawkes EW, Majidi C, Tolley MT. Hard questions for soft robotics. *Sci Robot* 2021;6:1–6.
9. Lu H, Hong Y, Yang Y, *et al.* Battery-less soft millirobot that can move, sense, and communicate remotely by coupling the magnetic and piezoelectric effects. *Adv Sci* 2020; 7:1–9.
10. Li S, Batra R, Brown D, *et al.* Particle robotics based on statistical mechanics of loosely coupled components. *Nature* 2019;567:361–365.
11. Ze Q, Kuang X, Wu S, *et al.* Magnetic shape memory polymers with integrated multifunctional shape manipulation. *Adv Mater* 2020;32:1–8.
12. Ng CSX, Tan MWM, Xu C, *et al.* Locomotion of miniature soft robots. *Adv Mater* 2021;33:1–24.

13. Wang Y, Yang X, Chen Y, *et al.* A biorobotic adhesive disc for underwater hitchhiking inspired by the remora suckerfish. *Sci Robot* 2017;2:1–10.
14. Koh J-S, Yang E, Jung G-P, *et al.* Jumping on water: surface tension-dominated jumping of water striders and robotic insects. *Science* (80-) 2015;349:517–521.
15. Hawkes EW, Blumenschein LH, Greer JD, *et al.* A soft robot that navigates its environment through growth. *Sci Robot* 2017;2:1–8.
16. Wu Y, Yim JK, Liang J, *et al.* Insect-scale fast moving and ultrarobust soft robot. *Sci Robot* 2019;4:eaax1594.
17. Liang J, Wu Y, Yim JK, *et al.* Electrostatic footpads enable agile insect-scale soft robots with trajectory control. *Sci Robot* 2021;6:1–12.
18. Li T, Zou Z, Mao G, *et al.* Agile and resilient insect-scale robot. *Soft Robot* 2018;00:soro.2018.0053.
19. Ortega-Jimenez VM, Von Rabenau L, Dudley R. Escape jumping by three age-classes of water striders from smooth, wavy & bubbling water surfaces. *J Exp Biol* 2017;220:2809–2815.
20. Jones TJ, Jambon-Puillet E, Marthelot J, *et al.* Bubble casting soft robotics. *Nature* 2021;599:229–233.
21. Wehner M, Truby RL, Fitzgerald DJ, *et al.* An integrated design and fabrication strategy for entirely soft, autonomous robots. *Nat Publ Gr* 2016;536:451–455.
22. Wang W, Han B, Zhang Y, *et al.* Laser-induced graphene tapes as origami and stick-on labels for photothermal manipulation via Marangoni effect. *Adv Funct Mater* 2021;31:1–11.
23. Huang X, Kumar K, Jawed MK, *et al.* Chasing biomimetic locomotion speeds: creating untethered soft robots with shape memory alloy actuators downloaded from. *Sci Robot* 2018;3:7557.
24. Kim Y, Yuk H, Zhao R, *et al.* Printing ferromagnetic domains for untethered fast-transforming soft materials. *Nature* 2018;558:274–279.
25. Hu W, Lum GZ, Mastrangeli M, *et al.* Small-scale soft-bodied robot with multimodal locomotion. *Nature* 2018;554:81–85.
26. Ke X, Zhang S, Chai Z, *et al.* Flexible discretely-magnetized configurable soft robots via laser-tuned selective transfer printing of anisotropic ferromagnetic cells. *Mater Today Phys* 2021;17:100313.
27. Gu G, Zou J, Zhao R, *et al.* Soft Wall-Climbing Robots. *Sci Robot* 2018;2874:1–13.
28. Gu G, Zhang N, Xu H, *et al.* A soft neuroprosthetic hand providing simultaneous myoelectric control and tactile feedback. *Nat Biomed Eng* 2021.
29. Pena-Francesch A, Giltinan J, Sitti M. Multifunctional and biodegradable self-propelled protein motors. *Nat Commun* 2019;10:1–10.
30. Lee KY, Park SJ, Matthews DG, *et al.* An autonomously swimming biohybrid fish designed with human cardiac biophysics. *Science* (80-) 2022;375:639–647.
31. Erb RM, Martin JJ, Soheilian R, *et al.* Actuating soft matter with magnetic torque. *Adv Funct Mater* 2016;26:3859–3880.
32. Diller E, Miyashita S, Sitti M. Remotely addressable magnetic composite micropumps. *RSC Adv* 2012;2:3850–3856.
33. Wang X, Mao G, Ge J, *et al.* Untethered and ultrafast soft-bodied robots. *Commun Mater* 2020;1:67.
34. Hong C, Ren Z, Wang C, *et al.* Magnetically actuated gearbox for the wireless control of millimeter-scale robots. *Sci Robot* 2022;7:eabo4401.
35. Zhang S, Ke X, Jiang Q, *et al.* Programmable and reprocessable multifunctional elastomeric sheets for soft origami robots. *Sci Robot* 2021;6:1–13.
36. Xu T, Zhang J, Salehizadeh M, *et al.* Millimeter-scale flexible robots with programmable three-dimensional magnetization and motions. *Sci Robot* 2019;4:eaav4494.
37. Lu H, Zhang M, Yang Y, *et al.* A bioinspired multilegged soft millirobot that functions in both dry and wet conditions. *Nat Commun* 2018;9:3944.
38. Yang X, Shang W, Lu H, *et al.* An agglutinate magnetic spray transforms inanimate objects into millirobots for biomedical applications. *Sci Robot* 2020;5:1–13.
39. Zhao R, Kim Y, Chester SA, *et al.* Mechanics of hard-magnetic soft materials. *J Mech Phys Solids* 2019;124:244–263.
40. Jiang J, Zhang S, Wang B, *et al.* Hydroprinted liquid-alloy-based morphing electronics for fast-growing/tender plants: from physiology monitoring to habit manipulation. *Small* 2020;16:1–10.
41. Zhang S, Jiang J, Jiang Q, *et al.* Dynamically conformal mask printing of liquid alloy circuits on morphing objects. *Adv Mater Technol* 2021;6:1–10.

Address correspondence to:

Zhiqiang Wu
State Key Laboratory of Digital
Manufacturing Equipment and Technology
Huazhong University of Science and Technology
Wuhan 430074
China

E-mail: zgwu@hust.edu.cn